

Measurements of WW and WZ production in $W + \text{jets}$ final states in $p\bar{p}$ collisions

V.M. Abazov,³⁴ B. Abbott,⁷² B.S. Acharya,²⁸ M. Adams,⁴⁸ T. Adams,⁴⁶ G.D. Alexeev,³⁴ G. Alkhalazov,³⁸ A. Alton^a,⁶⁰ G. Alverson,⁵⁹ G.A. Alves,² M. Aoki,⁴⁷ A. Askew,⁴⁶ B. Åsman,⁴⁰ S. Atkins,⁵⁷ O. Atramentov,⁶⁴ K. Augsten,⁹ C. Avila,⁷ J. BackusMayes,⁷⁹ F. Badaud,¹² L. Bagby,⁴⁷ B. Baldin,⁴⁷ D.V. Bandurin,⁴⁶ S. Banerjee,²⁸ E. Barberis,⁵⁹ P. Baringer,⁵⁵ J. Barreto,³ J.F. Bartlett,⁴⁷ U. Bassler,¹⁷ V. Bazterra,⁴⁸ A. Bean,⁵⁵ M. Begalli,³ C. Belanger-Champagne,⁴⁰ L. Bellantoni,⁴⁷ S.B. Beri,²⁶ G. Bernardi,¹⁶ R. Bernhard,²¹ I. Bertram,⁴¹ M. Besançon,¹⁷ R. Beuselinck,⁴² V.A. Bezzubov,³⁷ P.C. Bhat,⁴⁷ V. Bhatnagar,²⁶ G. Blazey,⁴⁹ S. Blessing,⁴⁶ K. Bloom,⁶³ A. Boehnlein,⁴⁷ D. Boline,⁶⁹ E.E. Boos,³⁶ G. Borissov,⁴¹ T. Bose,⁵⁸ A. Brandt,⁷⁵ O. Brandt,²² R. Brock,⁶¹ G. Brooijmans,⁶⁷ A. Bross,⁴⁷ D. Brown,¹⁶ J. Brown,¹⁶ X.B. Bu,⁴⁷ M. Buehler,⁴⁷ V. Buescher,²³ V. Bunichev,³⁶ S. Burdin^b,⁴¹ T.H. Burnett,⁷⁹ C.P. Buszello,⁴⁰ B. Calpas,¹⁴ E. Camacho-Pérez,³¹ M.A. Carrasco-Lizarraga,⁵⁵ B.C.K. Casey,⁴⁷ H. Castilla-Valdez,³¹ S. Chakrabarti,⁶⁹ D. Chakraborty,⁴⁹ K.M. Chan,⁵³ A. Chandra,⁷⁷ E. Chapon,¹⁷ G. Chen,⁵⁵ S. Chevalier-Théry,¹⁷ D.K. Cho,⁷⁴ S.W. Cho,³⁰ S. Choi,³⁰ B. Choudhary,²⁷ S. Cihangir,⁴⁷ D. Claes,⁶³ J. Clutter,⁵⁵ M. Cooke,⁴⁷ W.E. Cooper,⁴⁷ M. Corcoran,⁷⁷ F. Couderc,¹⁷ M.-C. Cousinou,¹⁴ A. Croc,¹⁷ D. Cutts,⁷⁴ A. Das,⁴⁴ G. Davies,⁴² K. De,⁷⁵ S.J. de Jong,³³ E. De La Cruz-Burelo,³¹ F. Déliot,¹⁷ R. Demina,⁶⁸ D. Denisov,⁴⁷ S.P. Denisov,³⁷ S. Desai,⁴⁷ C. Deterre,¹⁷ K. DeVaughan,⁶³ H.T. Diehl,⁴⁷ M. Diesburg,⁴⁷ P.F. Ding,⁴³ A. Dominguez,⁶³ T. Dorland,⁷⁹ A. Dubey,²⁷ L.V. Dudko,³⁶ D. Duggan,⁶⁴ A. Duperrin,¹⁴ S. Dutt,²⁶ A. Dyshkant,⁴⁹ M. Eads,⁶³ D. Edmunds,⁶¹ J. Ellison,⁴⁵ V.D. Elvira,⁴⁷ Y. Enari,¹⁶ H. Evans,⁵¹ A. Evdokimov,⁷⁰ V.N. Evdokimov,³⁷ G. Facini,⁵⁹ T. Ferbel,⁶⁸ F. Fiedler,²³ F. Filthaut,³³ W. Fisher,⁶¹ H.E. Fisk,⁴⁷ M. Fortner,⁴⁹ H. Fox,⁴¹ S. Fuess,⁴⁷ A. Garcia-Bellido,⁶⁸ G.A. García-Guerra^c,³¹ V. Gavrilov,³⁵ P. Gay,¹² W. Geng,^{14,61} D. Gerbaudo,⁶⁵ C.E. Gerber,⁴⁸ Y. Gershtein,⁶⁴ G. Ginther,^{47,68} G. Golovanov,³⁴ A. Goussiou,⁷⁹ P.D. Grannis,⁶⁹ S. Greder,¹⁸ H. Greenlee,⁴⁷ Z.D. Greenwood,⁵⁷ E.M. Gregores,⁴ G. Grenier,¹⁹ Ph. Gris,¹² J.-F. Grivaz,¹⁵ A. Grohsjean,¹⁷ S. Grünendahl,⁴⁷ M.W. Grünewald,²⁹ T. Guillemin,¹⁵ G. Gutierrez,⁴⁷ P. Gutierrez,⁷² A. Haas^d,⁶⁷ S. Hagopian,⁴⁶ J. Haley,⁵⁹ L. Han,⁶ K. Harder,⁴³ A. Harel,⁶⁸ J.M. Hauptman,⁵⁴ J. Hays,⁴² T. Head,⁴³ T. Hebbeker,²⁰ D. Hedin,⁴⁹ H. Hegab,⁷³ A.P. Heinson,⁴⁵ U. Heintz,⁷⁴ C. Hensel,²² I. Heredia-De La Cruz,³¹ K. Herner,⁶⁰ G. Hesketh^e,⁴³ M.D. Hildreth,⁵³ R. Hirosky,⁷⁸ T. Hoang,⁴⁶ J.D. Hobbs,⁶⁹ B. Hoeneisen,¹¹ M. Hohlfeld,²³ Z. Hubacek,^{9,17} V. Hynek,⁹ I. Iashvili,⁶⁶ Y. Ilchenko,⁷⁶ R. Illingworth,⁴⁷ A.S. Ito,⁴⁷ S. Jabeen,⁷⁴ M. Jaffré,¹⁵ D. Jamin,¹⁴ A. Jayasinghe,⁷² R. Jesik,⁴² K. Johns,⁴⁴ M. Johnson,⁴⁷ A. Jonckheere,⁴⁷ P. Jonsson,⁴² J. Joshi,²⁶ A.W. Jung,⁴⁷ A. Juste,³⁹ K. Kaadze,⁵⁶ E. Kajfasz,¹⁴ D. Karmanov,³⁶ P.A. Kasper,⁴⁷ I. Katsanos,⁶³ R. Kehoe,⁷⁶ S. Kermiche,¹⁴ N. Khalatyan,⁴⁷ A. Khanov,⁷³ A. Kharchilava,⁶⁶ Y.N. Kharzheev,³⁴ J.M. Kohli,²⁶ A.V. Kozelov,³⁷ J. Kraus,⁶¹ S. Kulikov,³⁷ A. Kumar,⁶⁶ A. Kupco,¹⁰ T. Kurča,¹⁹ V.A. Kuzmin,³⁶ J. Kvita,⁸ S. Lammers,⁵¹ G. Landsberg,⁷⁴ P. Lebrun,¹⁹ H.S. Lee,³⁰ S.W. Lee,⁵⁴ W.M. Lee,⁴⁷ J. Lellouch,¹⁶ L. Li,⁴⁵ Q.Z. Li,⁴⁷ S.M. Lietti,⁵ J.K. Lim,³⁰ D. Lincoln,⁴⁷ J. Linnemann,⁶¹ V.V. Lipaev,³⁷ R. Lipton,⁴⁷ Y. Liu,⁶ A. Lobodenko,³⁸ M. Lokajicek,¹⁰ R. Lopes de Sa,⁶⁹ H.J. Lubatti,⁷⁹ R. Luna-Garcia^f,³¹ A.L. Lyon,⁴⁷ A.K.A. Maciel,² D. Mackin,⁷⁷ R. Madar,¹⁷ R. Magaña-Villalba,³¹ S. Malik,⁶³ V.L. Malyshev,³⁴ Y. Maravin,⁵⁶ J. Martínez-Ortega,³¹ R. McCarthy,⁶⁹ C.L. McGivern,⁵⁵ M.M. Meijer,³³ A. Melnitchouk,⁶² D. Menezes,⁴⁹ P.G. Mercadante,⁴ M. Merkin,³⁶ A. Meyer,²⁰ J. Meyer,²² F. Miconi,¹⁸ N.K. Mondal,²⁸ G.S. Muanza,¹⁴ M. Mulhearn,⁷⁸ E. Nagy,¹⁴ M. Naimuddin,²⁷ M. Narain,⁷⁴ R. Nayyar,²⁷ H.A. Neal,⁶⁰ J.P. Negret,⁷ P. Neustroev,³⁸ S.F. Novaes,⁵ T. Nunnemann,²⁴ G. Obrant[‡],³⁸ J. Orduna,⁷⁷ N. Osman,¹⁴ J. Osta,⁵³ G.J. Otero y Garzón,¹ M. Padilla,⁴⁵ A. Pal,⁷⁵ N. Parashar,⁵² V. Parihar,⁷⁴ S.K. Park,³⁰ R. Partridge^d,⁷⁴ N. Parua,⁵¹ A. Patwa,⁷⁰ B. Penning,⁴⁷ M. Perfilov,³⁶ Y. Peters,⁴³ K. Petridis,⁴³ G. Petrillo,⁶⁸ P. Pétrouff,¹⁵ R. Piegai^a,¹ M.-A. Pleier,⁷⁰ P.L.M. Podesta-Lerma^g,³¹ V.M. Podstavkov,⁴⁷ P. Polozov,³⁵ A.V. Popov,³⁷ M. Prewitt,⁷⁷ D. Price,⁵¹ N. Prokopenko,³⁷ J. Qian,⁶⁰ A. Quadt,²² B. Quinn,⁶² M.S. Rangel,² K. Ranjan,²⁷ P.N. Ratoff,⁴¹ I. Razumov,³⁷ P. Renkel,⁷⁶ M. Rijssenbeek,⁶⁹ I. Ripp-Baudot,¹⁸ F. Rizatdinova,⁷³ M. Rominsky,⁴⁷ A. Ross,⁴¹ C. Royon,¹⁷ P. Rubinov,⁴⁷ R. Ruchti,⁵³ G. Safronov,³⁵ G. Sajot,¹³ P. Salcido,⁴⁹ A. Sánchez-Hernández,³¹ M.P. Sanders,²⁴ B. Sanghi,⁴⁷ A.S. Santos,⁵ G. Savage,⁴⁷ L. Sawyer,⁵⁷ T. Scanlon,⁴² R.D. Schamberger,⁶⁹ Y. Scheglov,³⁸ H. Schellman,⁵⁰ T. Schliephake,²⁵ S. Schlobohm,⁷⁹ C. Schwanenberger,⁴³ R. Schwienhorst,⁶¹ J. Sekaric,⁵⁵ H. Severini,⁷² E. Shabalina,²² V. Shary,¹⁷ A.A. Shchukin,³⁷ R.K. Shivpuri,²⁷ V. Simak,⁹ V. Sirotenko,⁴⁷ P. Skubic,⁷² P. Slattery,⁶⁸ D. Smirnov,⁵³ K.J. Smith,⁶⁶ G.R. Snow,⁶³ J. Snow,⁷¹ S. Snyder,⁷⁰

S. Söldner-Rembold,⁴³ L. Sonnenschein,²⁰ K. Soustruznik,⁸ J. Stark,¹³ V. Stolin,³⁵ D.A. Stoyanova,³⁷ M. Strauss,⁷² D. Strom,⁴⁸ L. Stutte,⁴⁷ L. Suter,⁴³ P. Svoisky,⁷² M. Takahashi,⁴³ A. Tanasijczuk,¹ M. Titov,¹⁷ V.V. Tokmenin,³⁴ Y.-T. Tsai,⁶⁸ K. Tschann-Grimm,⁶⁹ D. Tsybychev,⁶⁹ B. Tuchming,¹⁷ C. Tully,⁶⁵ L. Uvarov,³⁸ S. Uvarov,³⁸ S. Uzunyan,⁴⁹ R. Van Kooten,⁵¹ W.M. van Leeuwen,³² N. Varelas,⁴⁸ E.W. Varnes,⁴⁴ I.A. Vasilyev,³⁷ P. Verdier,¹⁹ L.S. Vertogradov,³⁴ M. Verzocchi,⁴⁷ M. Vesterinen,⁴³ D. Vilanova,¹⁷ P. Vokac,⁹ H.D. Wahl,⁴⁶ M.H.L.S. Wang,⁴⁷ J. Warchol,⁵³ G. Watts,⁷⁹ M. Wayne,⁵³ M. Weber,^{h, 47} L. Welty-Rieger,⁵⁰ A. White,⁷⁵ D. Wicke,²⁵ M.R.J. Williams,⁴¹ G.W. Wilson,⁵⁵ M. Wobisch,⁵⁷ D.R. Wood,⁵⁹ T.R. Wyatt,⁴³ Y. Xie,⁴⁷ R. Yamada,⁴⁷ W.-C. Yang,⁴³ T. Yasuda,⁴⁷ Y.A. Yatsunenko,³⁴ Z. Ye,⁴⁷ H. Yin,⁴⁷ K. Yip,⁷⁰ S.W. Youn,⁴⁷ J. Yu,⁷⁵ T. Zhao,⁷⁹ B. Zhou,⁶⁰ J. Zhu,⁶⁰ M. Zielinski,⁶⁸ D. Zieminska,⁵¹ and L. Zivkovic⁷⁴

(The D0 Collaboration*)

¹Universidad de Buenos Aires, Buenos Aires, Argentina

²LAFEX, Centro Brasileiro de Pesquisas Físicas, Rio de Janeiro, Brazil

³Universidade do Estado do Rio de Janeiro, Rio de Janeiro, Brazil

⁴Universidade Federal do ABC, Santo André, Brazil

⁵Instituto de Física Teórica, Universidade Estadual Paulista, São Paulo, Brazil

⁶University of Science and Technology of China, Hefei, People's Republic of China

⁷Universidad de los Andes, Bogotá, Colombia

⁸Charles University, Faculty of Mathematics and Physics,

Center for Particle Physics, Prague, Czech Republic

⁹Czech Technical University in Prague, Prague, Czech Republic

¹⁰Center for Particle Physics, Institute of Physics,

Academy of Sciences of the Czech Republic, Prague, Czech Republic

¹¹Universidad San Francisco de Quito, Quito, Ecuador

¹²LPC, Université Blaise Pascal, CNRS/IN2P3, Clermont, France

¹³LPSC, Université Joseph Fourier Grenoble 1, CNRS/IN2P3,

Institut National Polytechnique de Grenoble, Grenoble, France

¹⁴CPPM, Aix-Marseille Université, CNRS/IN2P3, Marseille, France

¹⁵LAL, Université Paris-Sud, CNRS/IN2P3, Orsay, France

¹⁶LPNHE, Universités Paris VI and VII, CNRS/IN2P3, Paris, France

¹⁷CEA, Irfu, SPP, Saclay, France

¹⁸IPHC, Université de Strasbourg, CNRS/IN2P3, Strasbourg, France

¹⁹IPNL, Université Lyon 1, CNRS/IN2P3, Villeurbanne, France and Université de Lyon, Lyon, France

²⁰III. Physikalisches Institut A, RWTH Aachen University, Aachen, Germany

²¹Physikalisches Institut, Universität Freiburg, Freiburg, Germany

²²II. Physikalisches Institut, Georg-August-Universität Göttingen, Göttingen, Germany

²³Institut für Physik, Universität Mainz, Mainz, Germany

²⁴Ludwig-Maximilians-Universität München, München, Germany

²⁵Fachbereich Physik, Bergische Universität Wuppertal, Wuppertal, Germany

²⁶Panjab University, Chandigarh, India

²⁷Delhi University, Delhi, India

²⁸Tata Institute of Fundamental Research, Mumbai, India

²⁹University College Dublin, Dublin, Ireland

³⁰Korea Detector Laboratory, Korea University, Seoul, Korea

³¹CINVESTAV, Mexico City, Mexico

³²Nikhef, Science Park, Amsterdam, the Netherlands

³³Radboud University Nijmegen, Nijmegen, the Netherlands and Nikhef, Science Park, Amsterdam, the Netherlands

³⁴Joint Institute for Nuclear Research, Dubna, Russia

³⁵Institute for Theoretical and Experimental Physics, Moscow, Russia

³⁶Moscow State University, Moscow, Russia

³⁷Institute for High Energy Physics, Protvino, Russia

³⁸Petersburg Nuclear Physics Institute, St. Petersburg, Russia

³⁹Institució Catalana de Recerca i Estudis Avançats (ICREA) and Institut de Física d'Altes Energies (IFAE), Barcelona, Spain

⁴⁰Stockholm University, Stockholm and Uppsala University, Uppsala, Sweden

⁴¹Lancaster University, Lancaster LA1 4YB, United Kingdom

⁴²Imperial College London, London SW7 2AZ, United Kingdom

⁴³The University of Manchester, Manchester M13 9PL, United Kingdom

⁴⁴University of Arizona, Tucson, Arizona 85721, USA

⁴⁵University of California Riverside, Riverside, California 92521, USA

⁴⁶Florida State University, Tallahassee, Florida 32306, USA

⁴⁷Fermi National Accelerator Laboratory, Batavia, Illinois 60510, USA

⁴⁸University of Illinois at Chicago, Chicago, Illinois 60607, USA

- ⁴⁹Northern Illinois University, DeKalb, Illinois 60115, USA
⁵⁰Northwestern University, Evanston, Illinois 60208, USA
⁵¹Indiana University, Bloomington, Indiana 47405, USA
⁵²Purdue University Calumet, Hammond, Indiana 46323, USA
⁵³University of Notre Dame, Notre Dame, Indiana 46556, USA
⁵⁴Iowa State University, Ames, Iowa 50011, USA
⁵⁵University of Kansas, Lawrence, Kansas 66045, USA
⁵⁶Kansas State University, Manhattan, Kansas 66506, USA
⁵⁷Louisiana Tech University, Ruston, Louisiana 71272, USA
⁵⁸Boston University, Boston, Massachusetts 02215, USA
⁵⁹Northeastern University, Boston, Massachusetts 02115, USA
⁶⁰University of Michigan, Ann Arbor, Michigan 48109, USA
⁶¹Michigan State University, East Lansing, Michigan 48824, USA
⁶²University of Mississippi, University, Mississippi 38677, USA
⁶³University of Nebraska, Lincoln, Nebraska 68588, USA
⁶⁴Rutgers University, Piscataway, New Jersey 08855, USA
⁶⁵Princeton University, Princeton, New Jersey 08544, USA
⁶⁶State University of New York, Buffalo, New York 14260, USA
⁶⁷Columbia University, New York, New York 10027, USA
⁶⁸University of Rochester, Rochester, New York 14627, USA
⁶⁹State University of New York, Stony Brook, New York 11794, USA
⁷⁰Brookhaven National Laboratory, Upton, New York 11973, USA
⁷¹Langston University, Langston, Oklahoma 73050, USA
⁷²University of Oklahoma, Norman, Oklahoma 73019, USA
⁷³Oklahoma State University, Stillwater, Oklahoma 74078, USA
⁷⁴Brown University, Providence, Rhode Island 02912, USA
⁷⁵University of Texas, Arlington, Texas 76019, USA
⁷⁶Southern Methodist University, Dallas, Texas 75275, USA
⁷⁷Rice University, Houston, Texas 77005, USA
⁷⁸University of Virginia, Charlottesville, Virginia 22901, USA
⁷⁹University of Washington, Seattle, Washington 98195, USA
- (Dated: December 1, 2011)

We study WW and WZ production with $\ell\nu qq$ ($\ell = e, \mu$) final states using data collected by the D0 detector at the Fermilab Tevatron Collider corresponding to 4.3 fb^{-1} of integrated luminosity from $p\bar{p}$ collisions at $\sqrt{s} = 1.96 \text{ TeV}$. Assuming the ratio between the production cross sections $\sigma(WW)$ and $\sigma(WZ)$ as predicted by the standard model, we measure the total WV ($V = W, Z$) cross section to be $\sigma(WV) = 19.6^{+3.2}_{-3.0} \text{ pb}$, and reject the background-only hypothesis at a level of 7.9 standard deviations. We also use b -jet discrimination to separate the WZ component from the dominant WW component. Simultaneously fitting WW and WZ contributions, we measure $\sigma(WW) = 15.9^{+3.7}_{-3.2} \text{ pb}$ and $\sigma(WZ) = 3.3^{+4.1}_{-3.3} \text{ pb}$, which is consistent with the standard model predictions.

PACS numbers: 14.70.Fm, 14.70.Hp, 13.85.Ni, 13.85.Qk

The study of the production of VV ($V = W, Z$) boson pairs provides an important test of the electroweak sector of the standard model (SM). In $p\bar{p}$ collisions at $\sqrt{s} = 1.96 \text{ TeV}$, the next-to-leading order (NLO) SM cross sections for these processes are $\sigma(WW) = 11.7 \pm 0.8 \text{ pb}$, $\sigma(WZ) = 3.5 \pm 0.3 \text{ pb}$ and $\sigma(ZZ) = 1.4 \pm 0.1 \text{ pb}$ [1]. Measuring a significant departure in cross section or devia-

tions in the predicted kinematic distributions would indicate the presence of anomalous gauge boson couplings [2] or new particles in extensions of the SM [3]. This analysis also provides a proving ground for the advanced analysis techniques used in low mass Higgs searches [4]. The production of VV in $p\bar{p}$ collisions at the Fermilab Tevatron Collider has been observed in fully leptonic decay modes [5] and more recently, in leptons+jets decay modes [6], where the combined $WW + WZ$ cross section was measured.

In this Letter, we report observation of the production of a W boson that decays leptonically in associated production with a second vector boson that decays hadronically ($WV \rightarrow \ell\nu qq$; $\ell = e^\pm$ or μ^\pm , and ν and q denote matter or anti-matter as appropriate). The data used for this analysis correspond to 4.3 fb^{-1} of integrated lumi-

*with visitors from ^aAugustana College, Sioux Falls, SD, USA, ^bThe University of Liverpool, Liverpool, UK, ^cUPIITA-IPN, Mexico City, Mexico, ^dSLAC, Menlo Park, CA, USA, ^eUniversity College London, London, UK, ^fCentro de Investigacion en Computacion - IPN, Mexico City, Mexico, ^gECFM, Universidad Autonoma de Sinaloa, Culiacán, Mexico, and ^hUniversität Bern, Bern, Switzerland. [†]Deceased.

osity collected between 2006 and 2009 by the D0 detector [7] at the Fermilab Tevatron Collider. The D0 detector dijet mass resolution for W/Z decays of $\approx 18\%$ results in significant overlap of $W \rightarrow qq$ and $Z \rightarrow qq$ dijet mass peaks. Therefore, we first consider WW and WZ simultaneously and measure the total WV cross section assuming the ratio of WW to WZ cross sections as predicted by the SM. We then apply b -jet identification to separate the WZ contribution, where the Z boson decays into $b\bar{b}$ pairs, from the dominant WW production.

Candidate events in the electron channel are required to satisfy a single electron trigger or a trigger requiring electrons and jets, which results in a combined trigger efficiency of $(98_{-3}^{+2})\%$ for the $e\nu qq$ event selection described below. A comprehensive suite of triggers in the muon channel, based on leptons, jets and their combination, achieves a trigger efficiency of $(95 \pm 5)\%$ for the $\mu\nu qq$ event selection.

To select $WV \rightarrow \ell\nu qq$ candidates, we require a single reconstructed electron (muon) with transverse momentum $p_T > 15$ GeV (20 GeV) and pseudorapidity $|\eta| < 1.1$ (2.0) [8], missing transverse energy $\cancel{E}_T > 20$ GeV, and two or three jets reconstructed using a cone algorithm [9]. The jets must have $p_T > 20$ GeV, $|\eta| < 2.5$, and at least two tracks within the jet cone [9] originating from the $p\bar{p}$ interaction vertex. Lepton candidates must be spatially matched to a track that originates from the primary $p\bar{p}$ interaction vertex and they must be isolated from energy depositions in the calorimeter and other tracks in the central tracking detector. To reduce background from processes that do not contain $W \rightarrow \ell\nu$, we require that the transverse mass [10] is $M_T^{\ell\nu}$ (GeV) $> 40 - 0.5\cancel{E}_T$. In addition, we restrict $M_T^{\mu\nu} < 200$ GeV to suppress muon candidates with poorly measured momenta.

Signal and most of the background processes are modeled with Monte Carlo (MC) simulation. The signal events are generated with PYTHIA [11] using CTEQ6L1 parton distribution functions (PDFs) [12] and include all SM decays. The fixed-order matrix element (FOME) generator ALPGEN [13] with CTEQ6L1 PDF is used to generate W +jets, Z +jets, and $t\bar{t}$ events. The FOME generator COMPHEP [14] is used to produce single top-quark MC samples with CTEQ6M PDF [12]. Both ALPGEN and COMPHEP are interfaced to PYTHIA for parton showering and hadronization. The MC events undergo a GEANT-based [15] detector simulation and are reconstructed using the same algorithms as used for D0 data. The effect of multiple $p\bar{p}$ interactions is included by overlaying data events from random beam crossings on simulated events. The next-to-NLO (NNLO) cross section is used to normalize the Z +jets (light and heavy-flavor jets) [16]. The approximate NNLO cross section [17] is used to normalize the $t\bar{t}$ samples, while the single top-quark MC samples are normalized to the approximate next-to-NNLO cross section [18]. The normalization of the W +jets MC sample (for all flavor con-

tributions) is determined from data. Additional NLO heavy-flavor corrections are calculated with MCFM [19] and applied to Z/W +heavy-flavor jets MC samples.

The multijet background in which a jet is misidentified as a prompt lepton is determined from data. For the muon channel, the multijet background is modeled with data that fail the muon isolation requirements, but pass all other selections. For the electron channel, the multijet background is estimated using a data sample containing events that pass less restrictive electron quality requirements. Both multijet samples are corrected for contributions from processes modeled by MC. The multijet normalizations are determined from fits to the $M_T^{\ell\nu}$ distributions and assigned uncertainties of 20%.

To identify b -quark jets, in particular those originating from $Z \rightarrow b\bar{b}$ decays, we use the D0 neural network (NN) b -tagging algorithm [20]. The NN is trained to separate light-flavor jets from heavy-flavor jets based on a combination of variables sensitive to the presence of tracks and vertices displaced from the primary $p\bar{p}$ interaction vertex. The NN outputs for the two highest p_T jets are then used as inputs to the final multivariate discriminant. We define non-overlapping 0, 1, and 2-tag sub-channels based on whether neither, only one, or both of the two highest p_T jets pass the least restrictive NN operating point, for which the b -jet identification efficiency and the light-flavor jet misidentification rate are approximately 80% and 10%. Scale factors are applied to the MC events to account for any difference in efficiency or misidentification rate between data and simulation.

The dominant background is W +jets and therefore the modeling of this process in ALPGEN and the corresponding sources of uncertainties were studied in detail. Comparison of ALPGEN with other generators [21] and with data shows discrepancies in jet η , dijet angular separation and the transverse momentum of the W boson candidate. Thus, data are used to correct these quantities in the ALPGEN W +jets and Z +jets samples before b -tagging is performed [22]. The possible bias in this procedure from the presence of the diboson signal in data is small, but is taken into account as a systematic uncertainty.

As the diboson events are generated with a LO generator, changes to the event kinematics and the acceptance due to a NLO and resummation effects are studied using events from the MC@NLO [23] interfaced to HERWIG [24] for parton showering and hadronization and using the CTEQ6M PDF set. Comparing kinematics at the generator level after final state radiation, we parameterize a two-dimensional correction matrix in the p_T of the diboson system and of the highest p_T boson. After applying this correction to our PYTHIA sample, we find good agreement with MC@NLO for all distributions studied. Half of the difference between the PYTHIA and MC@NLO predictions is used as systematic uncertainty on the diboson production model, accounting for the possible effects of higher order corrections beyond NLO and of different

TABLE I: Number of events for signal and each background after the combined fit of WV using the RF output distribution (with total uncertainties determined from the fit) and the number of events observed in data.

	Electron channel	Muon channel
Diboson signal	1725 ± 84	1465 ± 67
W/Z +light-flavor jets	37232 ± 1033	33516 ± 709
W/Z +heavy-flavor jets	5371 ± 608	4854 ± 490
$t\bar{t}$ and single top	1746 ± 127	1214 ± 86
Multijet	10630 ± 1007	1982 ± 384
Total predicted	56704 ± 635	43031 ± 531
Data	56698	43044

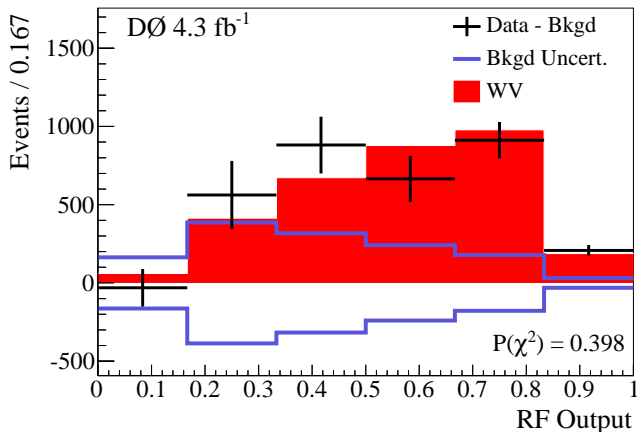


FIG. 1: (color online) A comparison of the measured WV signal (filled histogram) to background-subtracted data (points) in the RF output distribution (summed over electron and muon channels, and 0, 1, and 2-tag sub-channels), after the combined fit to data using the RF output distributions. Also shown is the ± 1 standard deviation uncertainty on the background prediction. The χ^2 fit probability, $P(\chi^2)$, is based on the residuals using data and MC statistical uncertainties.

showering scenarios.

The signal and the backgrounds are further separated using a multivariate classifier to combine information from several variables. This analysis uses a random forest (RF) classifier [25, 26], from which the output distribution is used as a final variable to measure the production cross sections by performing a template fit. Fifteen well-modeled variables [27] that demonstrate a difference in probability density between signal and at least one of the backgrounds are used as inputs to the RF. The RF is trained using a fraction of each MC sample. The remainder of each MC sample, along with the multijet background samples, is then evaluated by the RF and used in the measurement.

Depending on the source, we consider the effect of systematic uncertainty on the normalization and/or on the shape of differential distributions for signal and backgrounds [27]. Systematic effects on the differential distributions of the ALPGEN W +jets and Z +jets MC events

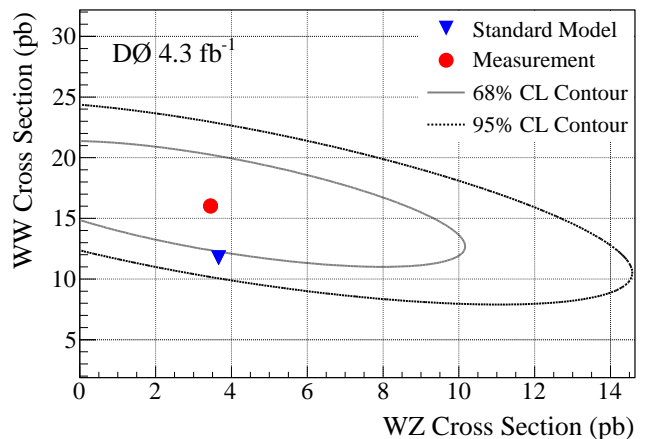


FIG. 2: (color online) Results from the simultaneous fit of $\sigma(WW)$ and $\sigma(WZ)$ using the RF output distributions. The plot shows the best fit value with 68% and 95% confidence level (CL) regions and the NLO SM prediction.

from changes of the renormalization and factorization scales and of the parameters used in the MLM parton-jet matching algorithm [28] are also considered. Uncertainties on PDFs [29], as well as uncertainties from object reconstruction and identification, are evaluated for all MC samples.

The total WV cross section is determined from a fit to the data of the signal and background RF output distributions. This fit is performed simultaneously on the distributions in the electron and muon channels, and in the 0, 1, and 2-tag sub-channels, by minimizing a Poisson χ^2 function with respect to variations in the systematic uncertainties [30]. The magnitude of the systematic uncertainties is effectively constrained by the regions of the RF output distribution with low signal over background ratio. A Gaussian prior is used for each systematic uncertainty. The effects on separate samples or sub-channels due to the same uncertainty are assumed to be 100% correlated. However, different uncertainties are assumed to be mutually independent.

The fit simultaneously varies the signal and W +jets contributions, thereby also determining the normalization factor for the W +jets MC sample. This obviates the need for using the predicted ALPGEN cross section, and provides a more rigorous approach that incorporates an unbiased uncertainty from W +jets when extracting the signal cross section. The W +jets normalization factor from the fit is consistent with the theoretical NNLO prediction [31]. The yields for signal and each background are given in Table I. Though the total diboson yield includes a small contribution from $ZZ \rightarrow \ell\ell q\bar{q}$ events (1.5%), in which one of the charged leptons escapes detection, the cross sections presented here are corrected for this contribution assuming that the ratios between WW , WZ and ZZ cross sections are given by the SM.

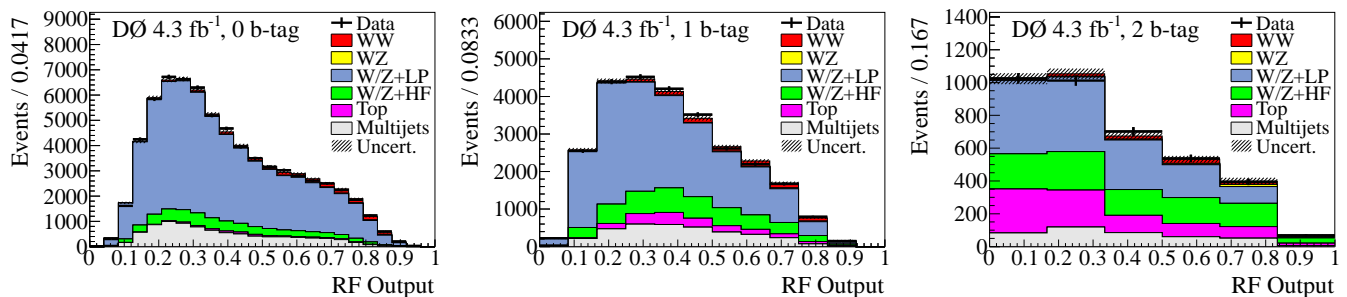


FIG. 3: (color online) A comparison of the signal+background prediction to data in the RF output distribution (summed over electron and muon channels) for 0, 1, and 2-tag sub-channels after the combined fit to data using the RF output distribution (LP denotes light partons such as u , d , s or gluon, and HF denotes heavy-flavor such as $c\bar{c}$ or $b\bar{b}$). The systematic uncertainty band is evaluated after the fit of the total WV cross section in the RF output distribution.

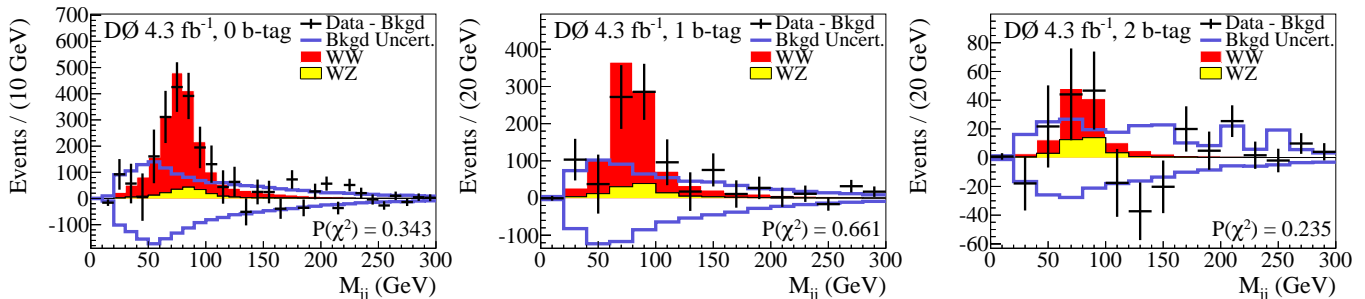


FIG. 4: (color online) A comparison of the measured WW and WZ signals (filled histograms) to background-subtracted data (points) in the dijet mass distribution (summed over electron and muon channels) for 0, 1, and 2-tag sub-channels after the combined fit to data using the dijet mass distribution. Also shown is the ± 1 standard deviation uncertainty on the background prediction. The χ^2 fit probability, $P(\chi^2)$, is based on the residuals using data and MC statistical uncertainties.

The fit of the total WV cross section using the RF output distributions yields $\sigma(WV) = 19.6^{+3.2}_{-3.0}$ pb, corresponding to an observed (expected) significance of 7.9 (5.9) standard deviations (s.d.). Figure 1 shows the background-subtracted RF output distribution summed over all sub-channels after the fit. As a cross check, we perform the measurement using the dijet mass distribution in place of the full RF output distribution [27]. This measurement yields a WV cross section of $\sigma(WV) = 18.3^{+3.8}_{-3.6}$ pb, consistent with that obtained using the RF output distribution.

The fit is then performed with the signal divided into the separate WW and WZ components, which are allowed to float independently. The result of this simultaneous fit of $\sigma(WW)$ and $\sigma(WZ)$ using the RF output distributions is shown in Fig. 2. It yields $\sigma(WW) = 15.9^{+1.9}_{-1.5}$ (stat) $^{+3.2}_{-2.9}$ (syst) pb and $\sigma(WZ) = 3.3^{+3.4}_{-2.7}$ (stat) $^{+2.2}_{-1.8}$ (syst) pb. The RF output distributions for the 0, 1, and 2-tag sub-channels from this fit are shown in Fig. 3. This measurement is also verified fitting the dijet mass distribution, which yields $\sigma(WW) = 13.3^{+2.8}_{-2.2}$ (stat) $^{+3.6}_{-2.9}$ (syst) pb and $\sigma(WZ) = 5.4^{+2.7}_{-2.6}$ (stat) $^{+4.5}_{-4.3}$ (syst) pb. Figure 4 shows plots for the background-subtracted dijet mass after the dijet mass fit.

We also perform a fit in which we constrain the WW

cross section to its SM prediction with a Gaussian prior equal to the theoretical uncertainty of 7% [1]. The fit of the RF output distribution yields a WZ cross section of $\sigma(WZ) = 6.5 \pm 0.9$ (stat) ± 3.0 (syst) pb with observed (expected) significance of 2.2 (1.2) s.d., and the dijet mass fit yields $\sigma(WZ) = 6.7 \pm 1.0$ (stat) ± 3.9 (syst) pb with observed (expected) significance of 1.7 (0.9) s.d. As expected, now that $\sigma(WW)$ is constrained to the SM prediction, the fit requires a higher rate for WZ in order to account for the excess of signal-like events.

In summary, we have measured the cross section for total WV production to be $\sigma(WV) = 19.6^{+3.2}_{-3.0}$ pb ($V = W$ or Z) with a significance of 7.9 s.d. above the background-only hypothesis. This result demonstrates the ability of the D0 experiment to measure a dijet signal in a background-dominated final state directly relevant to low mass Higgs searches. Furthermore, we have used b -jet tagging to measure the contributions from WW and WZ and measured the cross sections for the separate processes to be $\sigma(WW) = 15.9^{+3.7}_{-3.2}$ pb and $\sigma(WZ) = 3.3^{+4.1}_{-3.3}$ pb. Although we cannot yet claim 3 s.d. evidence of a WZ signal in the $lvjj$ final states, the extracted WV and WZ cross sections are in agreement with the SM prediction and their precise measurement represents an independent test to new physics which

could manifest itself differently in different final states.

We thank the staffs at Fermilab and collaborating institutions, and acknowledge support from the DOE and NSF (USA); CEA and CNRS/IN2P3 (France); FASI, Rosatom and RFBR (Russia); CNPq, FAPERJ, FAPESP and FUNDUNESP (Brazil); DAE and DST (India); Colciencias (Colombia); CONACyT (Mexico); KRF and KOSEF (Korea); CONICET and UBACyT (Argentina); FOM (The Netherlands); STFC and the Royal Society (United Kingdom); MSMT and GACR (Czech Republic); CRC Program and NSERC (Canada); BMBF and DFG (Germany); SFI (Ireland); The Swedish Research Council (Sweden); and CAS and CNSF (China).

-
- [1] J. M. Campbell and R. K. Ellis, Phys. Rev. D **60**, 113006 (1999). Cross sections are calculated with the same parameter values given in the Letter, except with $\sqrt{s} = 1.96$ TeV. We use MCFM version 6.0.
- [2] K. Hagiwara, S. Ishihara, R. Szalapski, and D. Zeppenfeld, Phys. Rev. D **48** (1993).
- [3] J. C. Pati and A. Salam, Phys. Rev. D **10**, 275 (1974); **11** 703(E) (1975); G. Altarelli, B. Mele, and M. Ruiz-Altaba, Z. Phys. C **45**, 109 (1989); **47**, 676(E) (1990); H. Davoudiasl, J. L. Hewett, and T. G. Rizzo, Phys. Rev. D **63**, 075004 (2001); H. He *et al.*, Phys. Rev. D **78**, 031701 (2008).
- [4] V. M. Abazov *et al.* (D0 Collaboration), Phys. Rev. Lett. **104**, 071801 (2010); V. M. Abazov *et al.* (D0 Collaboration), Phys. Rev. Lett. **105**, 251801 (2010); V. M. Abazov *et al.* (D0 Collaboration), Phys. Lett. B **698**, 6 (2011).
- [5] T. Aaltonen *et al.* (CDF Collaboration), Phys. Rev. Lett. **104**, 201801 (2010); V. M. Abazov *et al.* (D0 Collaboration), Phys. Lett. B **695**, 67 (2011); V. M. Abazov *et al.* (D0 Collaboration), Phys. Rev. D **84**, 011103 (2011).
- [6] T. Aaltonen *et al.* (CDF Collaboration), Phys. Rev. Lett. **103**, 091803 (2009); T. Aaltonen *et al.* (CDF Collaboration), Phys. Rev. Lett. **104**, 101801 (2010).
- [7] B. Abbott *et al.* (D0 Collaboration), Nucl. Instrum. Methods Phys. Res. A **565**, 463 (2006); M. Abolins *et al.*, Nucl. Instrum. and Methods A **584**, 75 (2007); R. Angstadt *et al.*, Nucl. Instrum. Methods Phys. Res. A **622**, 298 (2010).
- [8] D0 uses a spherical coordinate system with the z axis running along the proton beam axis. The angles θ and ϕ are the polar and azimuthal angles, respectively. Pseudorapidity is defined as $\eta = -\ln[\tan(\theta/2)]$, in which θ is measured with respect to the proton beam direction.
- [9] G. C. Blazey *et al.*, arXiv:hep-ex/0005012v2 (2000). The seeded cone algorithm with radius $\Delta\mathcal{R} = \sqrt{(\Delta\eta)^2 + (\Delta\phi)^2} = 0.5$ is used.
- [10] J. Smith, W. L. van Neerven, and J. A. M. Vermaseren, Phys. Rev. Lett. **50**, 1738 (1983).
- [11] T. Sjöstrand, S. Mrenna and P. Skands, J. High Energy Phys. **05**, 026 (2006). Version 6.409 is used.
- [12] J. Pumplin *et al.*, J. High Energy Phys. **07**, 12 (2002); J. Pumplin *et al.*, J. High Energy Phys. **10**, 46 (2003).
- [13] M. L. Mangano *et al.*, J. High Energy Phys. **07**, 001 (2003). Version 2.11 is used with the $W+c$ fix from v2.12.
- [14] E. Boos *et al.* (CompHEP Collaboration), Nucl. Instrum. Methods Phys. Res. A **534**, 250 (2004).
- [15] R. Brun, F. Carminati, CERN Program Library Long Writeup W5013 (1993).
- [16] R. Gavin, Y. Li, F. Petriello, and S. Quackenbush, Comput. Phys. Commun. **182**, 2388 (2011).
- [17] N. Kidonakis and R. Vogt, Phys. Rev. D **78**, 074005 (2008).
- [18] N. Kidonakis, Phys. Rev. D **74**, 114012 (2006).
- [19] J. M. Campbell and R. K. Ellis, Phys. Rev. D **65**, 113007 (2002).
- [20] V. M. Abazov *et al.* (D0 Collaboration), Nucl. Instrum. Methods Phys. Res. A **620**, 490 (2010).
- [21] J. Alwall *et al.*, Eur. Phys. C **53**, 473 (2008).
- [22] V. M. Abazov *et al.* (D0 Collaboration), Phys. Rev. Lett. **107**, 011804 (2011).
- [23] S. Frixione and B. R. Webber, J. High Energy Phys. **06**, 029 (2002); S. Frixione, P. Nason and B. R. Webber, J. High Energy Phys. **08**, 007 (2003). Version 3.3 is used.
- [24] G. Corcella *et al.*, J. High Energy Phys. **01**, 010 (2001).
- [25] L. Breiman, Machine Learning **45**, 5 (2001).
- [26] I. Narsky, arXiv:physics/0507143 (2005).
- [27] See Appendix.
- [28] S. Höche *et al.*, arXiv:hep-ph/0602031 (2006).
- [29] J. Pumplin *et al.*, Phys. Rev. D **65**, 014013 (2002).
- [30] W. Fisher, FERMILAB-TM-2386-E (2006).
- [31] R. Hamberg, W. L. van Neerven, and T. Matsuura, Nucl. Phys. B **359**, 343 (1991); **644**, 403 (2002).

APPENDIX

INPUT VARIABLES TO THE RANDOM FOREST CLASSIFIER

Here we define the fifteen variables used as inputs to the RF classifier. The observed distribution for each variable is shown in Figs. 5, 6 and 7 along with the predicted distribution after the fit of the total WV ($V = W, Z$) cross section using the RF output distribution.

The RF input variables can be classified into three categories: (i) b -jet identification variables, (ii) kinematics of individual final state particles, and (iii) kinematics of multiple final state particles. Several variables are calculated using the four-momentum of the dijet system, which we define as the sum of the four-momenta of the two highest p_T jets. We also reconstruct a $W \rightarrow \ell\nu$ candidate $W^{\ell\nu}$, from the charged lepton and the \cancel{E}_T . The neutrino from the $W \rightarrow \ell\nu$ decay is assigned the transverse momentum defined by \cancel{E}_T and a longitudinal momentum that is calculated assuming the mass of the $\ell\nu$ system is 80.4 GeV. Of the two possible solutions, we choose the real component that provides the smaller total invariant mass of all objects in the event.

- **b -jet Identification Variables:**

The NN b -tagger has 12 operating points characterized by different purities. Each jet is assigned an integer b -tag value based on the highest purity operating point that it passes.

1. Max b -tag Value: The greater b -tag value of the two highest p_T jets. The neural network b -tagger has 12 operating points of increasing purity and the b -tag value corresponds to the highest operating point satisfied by the jet (or zero if the jet did not satisfy any of the operating points).
2. Min b -tag Value: The lesser b -tag value of the two highest p_T jets.

These variables are shown in Fig. 5, both in logarithmic and linear scales.

- **Kinematics of Individual Final State Particles:**

1. $p_T(\ell)$: The p_T of the charged lepton.
2. $p_T(\text{jet}_1)$: The highest jet p_T .
3. $p_T(\text{jet}_2)$: The second highest jet p_T .
4. \cancel{E}_T : The imbalance in transverse energy determined from the energy measured in each calorimeter cell and then corrected for reconstructed muons, jets, and electrons/photons.

- **Kinematics of Multiple Final State Particles:**

1. M_{jj} : The invariant mass of the dijet system reconstructed from the two highest p_T jets.
2. $M_T^{\ell\nu} = \sqrt{2 p_T^\ell \cancel{E}_T (1 - \cos(\Delta\phi(\ell, \cancel{E}_T)))}$: The transverse W mass reconstructed from the charged lepton and the \cancel{E}_T .
3. $H_T = p_T(\text{jet}_1) + p_T(\text{jet}_2)$: The scalar sum of the two highest jet p_T s.
4. $p_T^{\text{rel}}(\text{dijet}, \text{jet}_1)^W = |\vec{p}_T(\text{jet}_1) \times \hat{p}_T(\text{jet}_1 + \text{jet}_2)|$: The magnitude of the leading jet transverse momentum perpendicular to the dijet system in the rest frame of the $W^{\ell\nu}$ candidate;
5. $p_T^{\text{rel}}(\text{dijet}, \text{jet}_2) = |\vec{p}_T(\text{jet}_2) \times \hat{p}_T(\text{jet}_1 + \text{jet}_2)|$: The magnitude of the second-leading jet transverse momentum perpendicular to the dijet system in the laboratory frame.
6. $k_T^{\text{min}} = \Delta R(\text{jet}_1, \text{jet}_2) \frac{p_T(\text{jet}_2)}{p_T(\ell) + \cancel{E}_T}$: The angular separation between the two jets of highest p_T , weighted by the ratio of the transverse momentum of the second-leading jet and a scalar sum of the transverse momenta of the $W^{\ell\nu}$ constituents.
7. $\cos(\angle(\text{dijet}, \text{jet}_1))$: The cosine of the angle between the momentum vectors of the dijet system and the highest p_T jet in the laboratory frame.
8. $\cos(\angle(W^{\ell\nu}, \text{jet}_1))^{jj}$: Cosine of the angle between the momentum vectors of the leading jet and the $W^{\ell\nu}$ candidate, evaluated in the rest frame of the dijet system.
9. Centrality: The scalar sum of transverse momenta of the charged lepton and all jets in the event divided by the sum of their energies.

SYSTEMATIC UNCERTAINTIES

Table II gives the size of the systematic uncertainties for Monte Carlo simulations and multijet estimates. We consider the effect of systematic uncertainties both on the normalization and on the shape of differential distributions for signal and backgrounds. Although Table II lists uncertainties for the diboson and W +jets simulation, these uncertainties are not used when measuring the diboson signal cross section, for which the diboson and W +jets normalizations are free parameters. However, the size of the uncertainty must be specified when estimating the significance and when we constrain the cross section for WW production to its SM prediction in the fit.

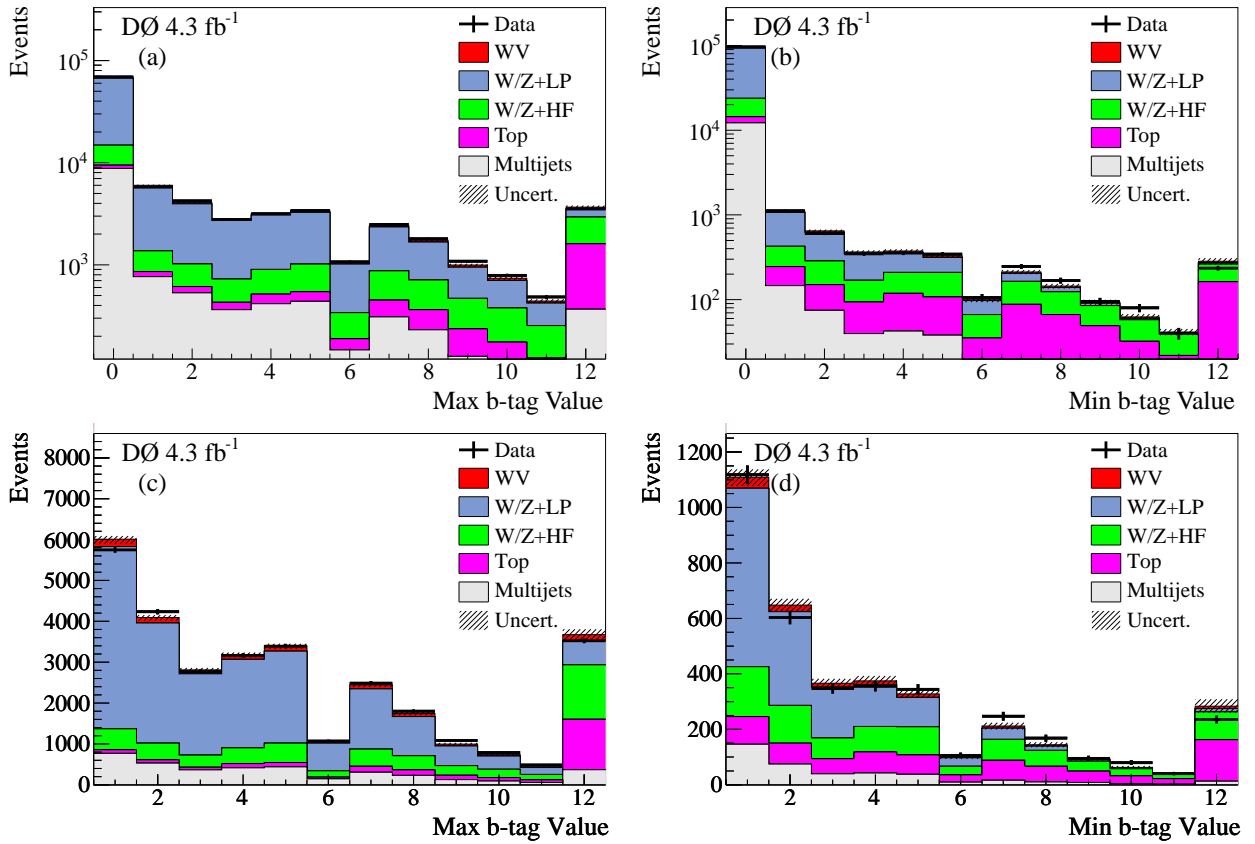


FIG. 5: (color online) Distributions of the b -jet identification variables used as inputs to the RF classifier (first two of fifteen) for electron and muon channels combined, with logarithmic ((a) and (b)) and linear ((c) and (d)) scales. To better show the WV and WZ signals the lowest bin is cut off in the distributions with a linear scale. The signal and background predictions and the systematic uncertainty band are evaluated after the fit of the total WV cross section in the RF output distribution. Definitions for each variable are provided in the text (LP denotes light partons such as u , d , s or gluon, and HF denotes heavy-flavor such as $c\bar{c}$ or $b\bar{b}$).

$\Delta\chi^2$ FOR WV MEASUREMENT

The statistical significance of the diboson signal yield from the fit to the data is estimated via analysis of the $\Delta\chi^2$ curve obtained by fitting the data to the sum of background and signal templates as a function of the signal rate. The results of this analysis are given in Table III. Figure 8 shows how the χ^2 of the fit changes as a function of the signal cross section when using either the dijet mass or the RF output distribution to measure the total WV cross section.

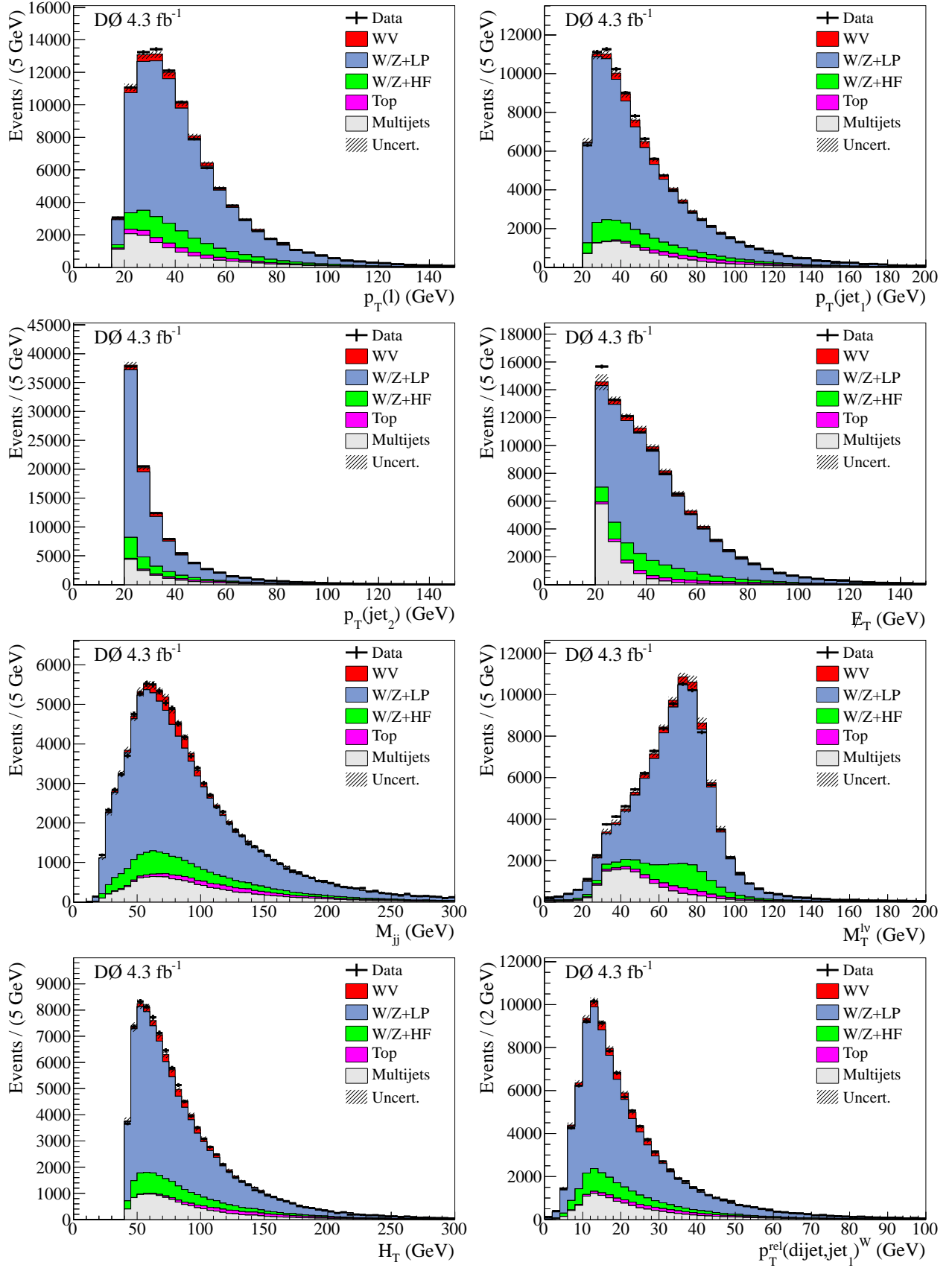


FIG. 6: (color online) Distributions of the variables (next eight of fifteen) used as inputs to the RF classifier for electron and muon channels combined, and before b -tagging. The signal and background predictions and the systematic uncertainty band are evaluated after the fit of the total WV cross section in the RF output distribution. Definitions for each variable are provided in the text (LP denotes light partons such as u , d , s or gluon, and HF denotes heavy-flavor such as $c\bar{c}$ or $b\bar{b}$).

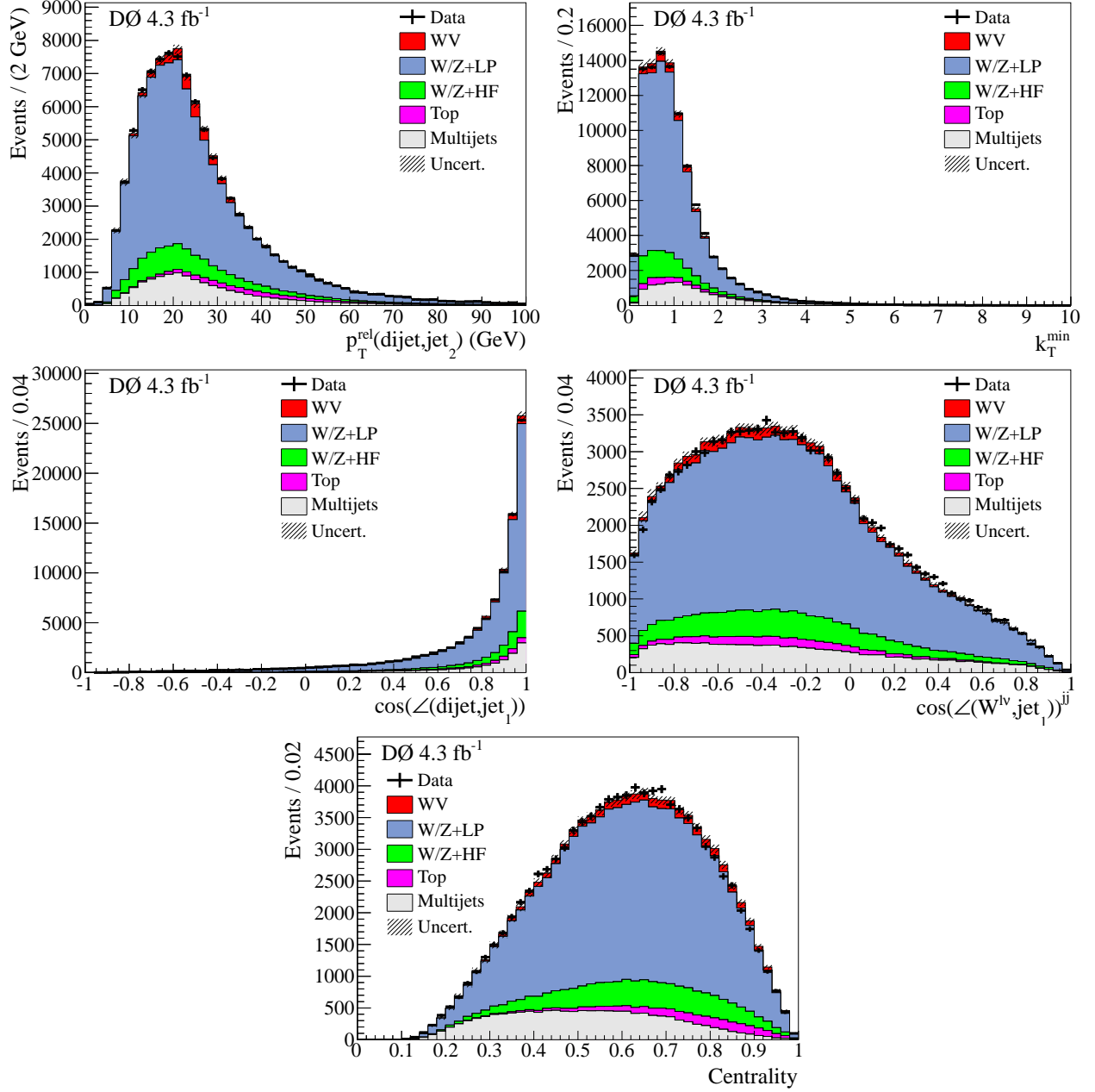


FIG. 7: (color online) Distributions of the variables (remaining five of fifteen) used as inputs to the RF classifier for electron and muon channels combined, and before b -tagging. The signal and background predictions and the systematic uncertainty band are evaluated after the fit of the total WV cross section in the RF output distribution. Definitions for each variable are provided in the text (LP denotes light partons such as u , d , s or gluon, and HF denotes heavy-flavor such as $c\bar{c}$ or $b\bar{b}$).

TABLE II: The RMS amplitude (in percent) of each systematic uncertainty in the RF output distributions for the signal and background predictions. The RMS amplitude is defined as: $\sqrt{\sum_{i=0}^n p_i \Delta_i^2 / \sum_{i=0}^n p_i}$; where p_i is the predicted number of events in bin i , Δ_i is the percent change in bin i when the uncertainty is varied by 1 s.d., and n is the number of bins. In cases where the amplitude is different for different subchannels, the range of amplitudes is given. The rightmost column indicates whether the uncertainty only affects the normalization (N) or if it has also a differential dependence (D).

Source of systematic uncertainty	Diboson signal	W +jets	Z +jets	Top	Multijet	Nature
Electron trigger/ID efficiency	± 5	± 5	± 5	± 5		N
Muon trigger/ID efficiency	± 5	± 5	± 5	± 5		N
Jet identification	± 1	$\pm 1-2$	$\pm 1-2$	$\pm <1-2$		D
Jet energy scale	$\pm 2-4$	$\pm 6-8$	$\pm 4-12$	$\pm 2-3$		D
Jet energy resolution	$\pm 2-3$	$\pm 3-12$	$\pm 4-10$	$\pm 1-2$		D
Jet vertex confirmation	$\pm 2-3$	$\pm 3-4$	$\pm 3-5$	$\pm 1-3$		D
Taggability correction	$\pm <1$	$\pm <1$	$\pm <1$	$\pm <1$		D
b -tagging	$\pm 1-5$	$\pm 1-4$	$\pm 1-5$	$\pm 8-10$		D
Luminosity	± 6.1	± 6.1	± 6.1	± 6.1		N
Cross section	± 7	± 6.3	± 6.3	± 10		N
V +heavy-flavor cross section		± 20	± 20			N
$V+2$ jets/ $V+3$ jets cross section		± 10	± 10			N
Multijet normalization					± 20	N
Multijet shape, electron channel					$\pm <1$	D
Multijet shape, muon channel					$\pm <1$	D
Diboson modeling	$\pm 2-3$					D
Parton distribution function	± 1	± 2	$\pm 1-3$	$\pm 2-4$		D
Unclustered Energy correction	$\pm <1$	$\pm <1$	$\pm <1$	$\pm <1$		D
ALPGEN jet η corrections		$\pm <1$	$\pm <1$			D
ALPGEN $\Delta R(jj)$ and $p_T(W)$ corrections		$\pm <1$	$\pm <1$			D
Re-weighting diboson bias		$\pm <1$	$\pm <1$	$\pm <1$		D
Renormalization and factorization scales		$\pm <1$	$\pm <1$			D
Underlying event model		$\pm <1$	± 1			D
ALPGEN parton-jet matching parameters		$\pm <1$	$\pm <1$			D

TABLE III: Results from fitting the total WV cross section and the uncertainties resulting from limited data statistics (stat), and possible systematic biases (syst). Also, the expected and observed $\Delta\chi^2$ obtained by fitting the data with and without the specified signal process and the corresponding significance in number of standard deviations (s.d.) for a one-sided Gaussian integral.

	Measured $\sigma(WV)$ [pb]	$\Delta\chi^2$ (significance)	
		Expected	Observed
RF Output	19.6 ± 1.4 (stat) $^{+2.9}_{-2.7}$ (syst)	35.8 (5.9 s.d.)	63.5 (7.9 s.d.)
Dijet Mass	18.3 ± 1.5 (stat) $^{+3.5}_{-3.3}$ (syst)	22.1 (4.6 s.d.)	33.0 (5.6 s.d.)

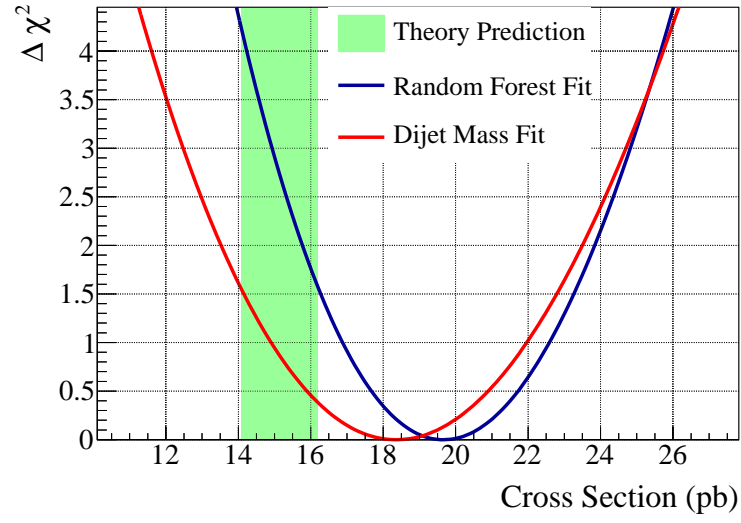


FIG. 8: (color online) The change in χ^2 relative to the best fit value when fitting the total WV cross section using either the dijet mass or the RF output distribution.